

MOX–Report No. 13/2012

**Global Sensitivity Analysis through Polynomial Chaos
Expansion of a basin-scale geochemical compaction
model**

FORMAGGIA, L.; GUADAGNINI, A.; IMPERIALI, I.;
LEVER, V.; PORTA, G.; RIVA, M.; SCOTTI, A.;
TAMELLINI, L.

MOX, Dipartimento di Matematica “F. Brioschi”
Politecnico di Milano, Via Bonardi 9 - 20133 Milano (Italy)

mox@mate.polimi.it

<http://mox.polimi.it>

Global Sensitivity Analysis through Polynomial Chaos Expansion of a basin-scale geochemical compaction model

Luca Formaggia* Alberto Guadagnini** Ilaria Imperiali*
Valentina Lever** Giovanni Porta** Monica Riva**
Anna Scotti* Lorenzo Tamellini*

February 2, 2012

* MOX– Modellistica e Calcolo Scientifico
Dipartimento di Matematica “F. Brioschi”
Politecnico di Milano
via Bonardi 9, 20133 Milano, Italy

** DIIAR,
Politecnico di Milano
Piazza Leonardo Da Vinci 32, 20133 Milano, Italy

Keywords: global sensitivity analysis, sedimentary basin evolution, polynomial chaos expansion, sparse grids sampling.

Abstract

We present a model-driven uncertainty quantification methodology based on the use of sparse grids sampling techniques in the context of a generalized Polynomial Chaos Expansion (GPCE) approximation of a basin-scale geochemical evolution scenario. The approach is illustrated through a one-dimensional example involving the process of quartz cementation in sandstones and the resulting effects on the dynamics of the vertical distribution of porosity, pressure and temperature. The proposed theoretical framework and computational tools allow performing an efficient and accurate Global Sensitivity Analysis (GSA) of the system states (i.e., porosity, temperature, pressure and fluxes) in the presence of uncertain key mechanical and geochemical model parameters as well as boundary conditions. GSA is grounded on the use of the variance-based Sobol indices. These allow discriminating the relative weights of uncertain quantities on the global model variance and can be computed through the GPCE of the model response surface. Evaluation of the GPCE of the random model response is performed through the implementation of a sparse grid interpolation technique in the space of the selected uncertain quantities. As opposed to a

standard Monte Carlo sampling, the use of sparse grids polynomial interpolants renders computationally affordable and reliable evaluations of the required indices. GPCE can then be employed as a surrogate model of the system states to quantify uncertainty propagation through the model in terms of the probability distribution (and its statistical moments) of target system states.

1 Introduction

Porosity dynamics observed in sedimentary basins has been ascribed mostly to mechanical compaction. This mechanism is effective during the early burial phase and was assumed to be responsible of cementation processes observed at the largest depth. This assumption is controversial because experimental observations are not entirely consistent with the idea that reduction of effective stresses at the onset of overpressure should stop porosity reduction.

Recent studies relate the diagenetic porosity reduction which is observed beyond a certain depth to temperature rather than to effective stress [1, 7, 30, 43], because of the relevance of the effects of temperature-activated reactions.

In this context, quartz precipitation in sandstones and smectite-illite transformation in shales are considered as key geochemical compaction processes driving basin scale evolution [9, 33, 27, 11]. Pressure solution is also a relevant mechanism in the presence of limestones and chalks, see e.g. [9, 27]. The complex mineralogic composition of natural rocks might result in the simultaneous occurrence of these reaction processes, with different relative importance within a region of interest. Here, we focus on the study of quartz cementation in sandstones, and its effect on the porosity and overpressure dynamics along the vertical direction.

Quartz cementation can be described as a sequence of three phases: dissolution of quartz grains, diffusion of the dissolved products, and precipitation. Precipitation is regarded as the rate limiting process (see e.g. [29]).

Some conceptual models of quartz cementation at the basin scale [38, 32, 28, 45] rely on the idea that cementation is the consequence of an intergranular pressure solution process. These models are mostly applied to calcite cementation rather than sandstones. A very detailed model to describe crystals growth is described in [19], taking into account the joint occurrence of several mineral species, equilibrium and kinetic reactions, and diffusive, dispersive and advective mass fluxes. This model requires the joint solution of the fluid flow field and temperature distribution and its complexity renders it unsuitable for large scale applications. Nevertheless, it has provided useful insights to detect the source of precipitated silica, suggesting that this should be internal to the system. We note that the assessment of the source of silica driving these processes is still not completely clear. According to some authors, [19, 47] the source of quartz is internal to the sandstone system and is related to pore scale reactions, pressure solution and smectite-illite transformation. The assumption of the action of an

external source of silica seems less likely, as this does not explain the strength of the cementation which is observed in nature [23, 8].

A simple empirical model for quartz precipitation is proposed in [42]. This model assumes that the source of quartz is local, and the dissolution at the solid grains boundary and diffusive processes are associated with time scales which are much shorter than those related to precipitation, thus having negligible effects at basin scale. The rate of precipitation is controlled by temperature ([41]) with an exponential dependence

$$R = a_q 10^{b_q T} \quad (1)$$

R being the precipitation rate per unit surface of the host rock. Here, T is temperature and a_q and b_q are two empirical constants that need to be calibrated against experimental data. The total volume of precipitated quartz then depends on temperature (note that precipitation is activated when $T > T_c$, T_c being a critical activation temperature) and the specific surface of the quartz matrix. Here, we consider the quartz cementation model (1) to describe geochemical compaction due to the coupled effects of quartz cementation and mechanical compaction. The equations describing the dynamic evolution of the system involve a number of parameters: these include the physical properties of the liquid phase and the host matrix, chemical parameters, as well as geological information about the system. Estimates of most of these parameters are corrupted by uncertainty, mainly due to difficulties related to obtain direct and reliable measurements of the quantities of interest at the spatial and temporal scales characterizing a basin compaction process. The relevance of these uncertainties has been previously documented in [24], where a sensitivity analysis of the problem is performed within a Monte Carlo scheme.

In this study we present a theoretical framework and associated computational tools for the efficient and accurate global sensitivity study of a basin evolution model in the presence of uncertain key mechanical and geochemical system parameters. We then adopt this procedure to

- (i) quantify the global uncertainty of the model state variables (including porosity, temperature and pressure heads) due to a set of uncertain input parameters and boundary conditions;
- (ii) identify the relative contribution of each selected uncertain quantity on the global uncertainty of the target state variables;
- (iii) assess propagation of uncertainty to the model response in terms of the space-time evolution of the probability density function (pdf) associated with the selected state variables.

A review of sensitivity analysis theoretical frameworks can be found in [34], where it is shown that a nonlinear model typically requires a global sensitivity analysis procedure. For our purposes, we select the variance-based Sobol sensitivity indices [37, 2, 34, 39]. These indices allow to evaluate the relative influence

of different uncertain parameters on the global model variance without the need for assuming any regularity of the underlying mathematical model.

As shown in [25, 39] the Sobol indices can be easily computed starting from a generalized polynomial chaos expansion (GPCE) of the solution as a function of the input parameters, i.e. an expansion in orthogonal polynomials of the input parameters, see e.g. [46, 18, 48]. Such a (truncated) GPCE can also be seen as a reduced model for the input/output mapping and can also be used to perform a Monte Carlo analysis of the system to assess propagation of uncertainty through the model at a significantly reduced computational cost (see e.g. [16], and references therein).

The global sensitivity analysis is developed according to the following three main steps.

1. *Parameter selection.* Identification of the parameter space of interest entails selecting the main uncertain quantities driving the model response, together with the corresponding probability distribution (e.g. Gaussian, uniform) and the related parameters (e.g. mean and standard deviation for a Gaussian distribution, or lower and upper bounds for a uniform distribution).
2. *Model evaluation.* The model response is calculated at different locations (collocation points) in the uncertain parameters space. The choice of the collocation points is (in principle) arbitrary and can be performed according to different strategies. For example, a standard Monte Carlo sampling of the collocation points considers a random selection in the parameter space. This strategy has been applied to a wide range of problems and provides robust results. It is computationally expensive as the number of collocation points needed to obtain reasonable accuracy for the quantities of interest is in general very large. To reduce the computational effort while keeping accurate results, we explore the use of the sparse grid interpolation method introduced in [36, 5, 12].
3. *Computation of sensitivity indices.* The sparse grid interpolant is converted into the GPCE reduced model of the solution and the required statistical indices (mean, standard deviation, Sobol indices) are computed. This approach to compute a GPCE expansion is relatively new and only few similar works are available in literature (e.g., [14]).

To the best of our knowledge, the adoption of Sobol indices within the context of a GPCE-based surrogate model for uncertainty quantification of sedimentary basins evolution has not been previously documented in the literature. It is also emphasized that computing the GPCE reduced model of a random function starting from a sparse grid interpolation represents a novel approach to the GPCE computation.

The paper is organized as follows. Section 2 presents the mathematical formulation of the problem and the parameters involved. Section 3 illustrates

the numerical methodology implemented to solve the basin compaction process. Section 4 is devoted to the description of the sensitivity analysis procedure. Results related to a selected test case are presented in Section 5.

2 Mathematical model

We consider a one-dimensional domain

$$\Omega(t) = (z_{bot}(t), z_{top}(t))$$

evolving with time, t , $z_{bot}(t)$ and $z_{top}(t)$ being the vertical locations of the basin basement and the ocean floor, respectively. Upon setting $z = 0$ at the sea level, we assume that the time evolution of $z_{top}(t)$ is provided on the basis of paleobathymetry data, while $z_{bot}(t)$ is calculated from solid mass conservation. The mathematical model for the coupled problem of geomechanical compaction and fluid flow in the one-dimensional domain is provided in the following Sections.

2.1 The Darcy's law

We assume that the fluid-phase velocity is provided through Darcy's law, i.e.

$$u^D = \phi(u^l - u^s) = -\frac{K}{\mu^l} \left(\frac{\partial p^l}{\partial z} - \rho^l g \right). \quad (2)$$

Here, u^D is Darcy flux, ϕ is the porosity of the sediments and superscripts l and s refer to fluid and solid phases, respectively. In particular, u^l and u^s indicate the velocities of the fluid and solid matrix, respectively, p^l the pore pressure, while ρ^l and μ^l the fluid density and dynamic viscosity, here considered constant for simplicity. Permeability K is considered as isotropic and is modeled as a function of porosity as

$$K = 10^{k_1 \phi - k_2 - \chi}, \quad (3)$$

where k_1 , k_2 are experimental parameters ([44]) and χ is a conversion factor from millidarcy unit (mD). In this work we have set $\chi = 15$.

2.2 Mass conservation

Mass conservation of the fluid and the solid phases in $\Omega(t)$ is governed by

$$\begin{aligned} \frac{\partial \phi \rho^l}{\partial t} + \frac{\partial (\phi \rho^l u^l)}{\partial z} &= q^l, \\ \frac{d}{dt} [(1 - \phi) \rho^s] + (1 - \phi) \rho^s \frac{\partial u^s}{\partial z} &= q_Q. \end{aligned} \quad (4)$$

The source term q^l accounts for processes associated with fluid generation, e.g. water release during transformation of clay minerals, and is neglected in our

study as we only consider sandstone compaction. The source term q_Q in the solid mass balance accounts for quartz precipitation. We have indicated with

$$\frac{d\cdot}{dt} = \frac{\partial\cdot}{\partial t} + u^s \frac{\partial\cdot}{\partial z},$$

the material derivative w.r.t. the solid matrix.

Darcy's law (2) and fluid mass conservation (4) constitute an elliptic problem (in mixed form) in the unknowns u^l and p^l . It must be complemented by appropriate boundary conditions. Here, we impose a given pressure p_{sea} at the top of the basin and assume that the bottom is impermeable.

The velocity u^s of the solid phase at the top of the basin is taken to be known on the basis of estimates of paleobathymetry and sedimentation rate.

2.3 Force balance

Let us define the overburden load $S(z)$ as

$$S(z) = \int_{z_{\text{top}}}^z - [\phi \rho^l + (1 - \phi) \rho^s] g dz + S_0, \quad (5)$$

where S_0 accounts for the weight of the water column in a submerged basin. The solid matrix is subject to an effective stress

$$\sigma = S(z) - p^l(z). \quad (6)$$

2.4 Compaction modelling

Porosity change depends on mechanical and geochemical processes. Purely mechanical compaction can be described by the following constitutive law

$$\phi_M = (\phi_0 - \phi_f) \exp(-\beta\sigma) + \phi_f, \quad (7)$$

where ϕ_0 is the initial porosity of the sediments, ϕ_f is the limiting value of porosity that can be attained by pure mechanical compaction, i.e. the void space that corresponds to the optimal packing of the grains, and β is the soil compressibility coefficient. According to (7), porosity decreases from ϕ_0 to ϕ_f with increasing effective stress σ . The rate of porosity change due to mechanical compaction is then given by

$$\frac{d\phi_M}{dt} = -\beta(\phi_0 - \phi_f) \exp(-\beta\sigma) \frac{d\sigma}{dt}. \quad (8)$$

We employ the following empirical model [42] to describe the kinetics of the quartz precipitation process

$$\frac{d\phi_Q}{dt} = \frac{M_Q}{\rho_Q} AR, \quad T > T_{\text{crit}}. \quad (9)$$

Here, ϕ_Q is the volumetric fraction of quartz cement, and M_Q and ρ_Q are the molar mass and the density of quartz, respectively. The reaction takes place only if the temperature is sufficiently high, $T > T_{\text{crit}} \simeq 80^\circ\text{C}$. The rate of quartz precipitation R is expressed as a function of temperature, T , while the surface A available for mineral deposition is modelled as a function of the porosity according to

$$R(T) = a_q 10^{b_q T}, \quad \text{and } A = A_0 \left(\frac{\phi}{\phi_{act}} \right), \quad (10)$$

A_0 and ϕ_{act} representing the specific surface and the actual porosity at the onset of quartz precipitation, respectively. The effects of mechanical and geochemical compaction are combined in the following relationship for porosity evolution

$$\frac{d\phi}{dt} = \frac{d\phi_M}{dt} - \frac{d\phi_Q}{dt}, \quad \phi \geq \phi_{min} > 0 \quad (11)$$

where $\frac{d\phi_M}{dt}$ and $\frac{d\phi_Q}{dt}$ are provided by (8) and (9), respectively. Here, ϕ_{min} is a small limiting value for the porosity.

2.5 Temperature dynamics

Temperature plays a key role in triggering geochemical compaction and its field evolution is modeled according to

$$C_T \frac{\partial T}{\partial t} + \left(\phi \rho^l c^l u^l + (1 - \phi) \rho^s c^s u^s \right) \frac{\partial T}{\partial z} - \frac{\partial}{\partial z} \left(K_T \frac{\partial T}{\partial z} \right) = Q, \quad (12)$$

where $C_T(\phi) = \phi \rho^l c^l + (1 - \phi) \rho^s c^s$ is the effective thermal capacity of the medium. Equation (12) can be re-written in a Lagrangian framework using (2)

$$C_T \frac{dT}{dt} + \left(\rho^l c^l u^D \right) \frac{\partial T}{\partial z} - \frac{\partial}{\partial z} \left(K_T \frac{\partial T}{\partial z} \right) = Q. \quad (13)$$

The thermal conductivity K_T of the water/rock system depends on temperature according to

$$K_T(T) = \lambda_f^\phi [\lambda_s(T)]^{1-\phi} \quad \lambda_s(T) = \frac{\lambda_0}{1 + c_0 T},$$

and introduces a non-linear term in the heat equation. Here λ_f and λ_s represent fluid and solid specific conductivities respectively, λ_0 is a reference conductivity at $T = 0^\circ\text{C}$ and c_0 an experimental parameter. Finally, Q models the possible occurrence of internal heat sources, and it is neglected in the following. As boundary condition, we prescribe a temperature value at the top of the basin and impose a given heat flux at the bottom. We consider that a linear temperature profile, $T_0(z)$, develops within the system at the initial simulation time, according to a typical geothermal gradient.

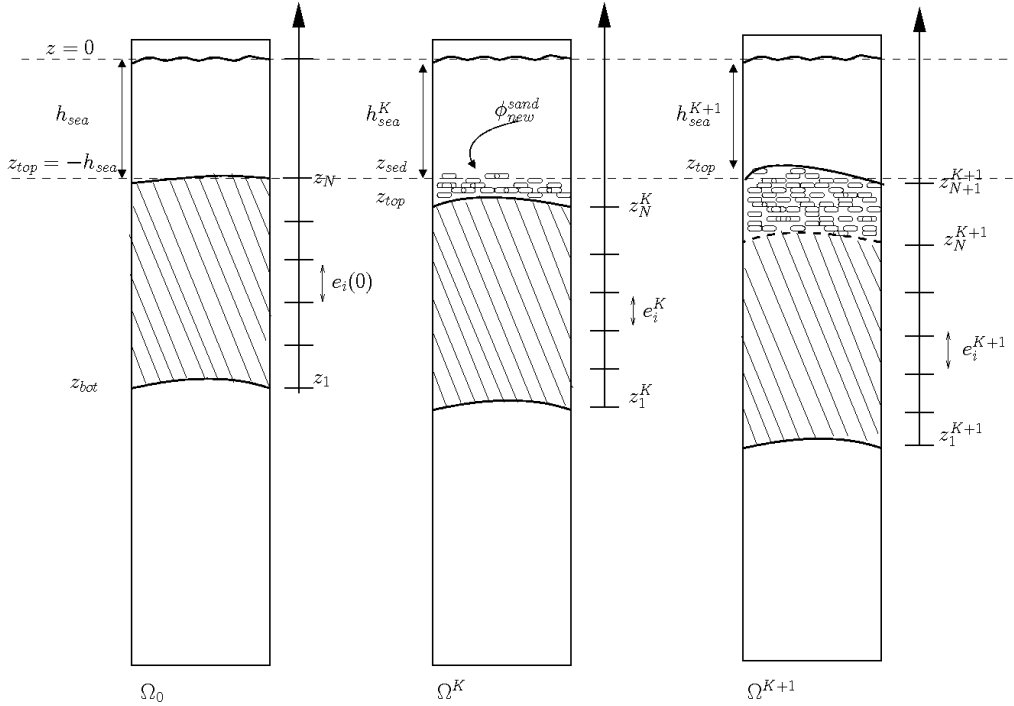


Figure 1: Frame of reference and discretization of the one-dimensional, time dependent domain considered.

3 Numerical solution

This section illustrates the iterative method adopted for the solution of the system of coupled differential equations presented in Section 2. Their distinctive characteristic is the presence of an evolving domain and the occurrence of strong non-linearities.

3.1 Lagrangian approach

A Lagrangian approach where the computational grid is deformed under the effect of compaction according to the solid matrix movement is adopted to address the temporal evolution of the computational domain. In this framework, each cell is formed always by the same portion of solid material, so that no transfer of solid mass occurs between two different cells. The heat and fluid flow equations are thus expressed in terms of material derivatives, avoiding the need of introducing advection terms.

In our problem setting, the domain and the grid deform under the effect of sedimentation, to include the deposition of new sediment layers over time, and possibly erosion. There are two different ways of taking into account the sedimentation of new material. A first approach relies on adding a new cell

at the top of the mesh at each sedimentation event, increasing the size of the the computational domain. Alternatively, newly accumulated sediments can be considered as an additional time-varying load acting at the top of the basin, inducing time-dependent boundary conditions for the pressure and temperature equations.

In our work we use a hybrid technique which describes sedimentation by a modified load until the thickness of fresh sediments equals the characteristic size of the mesh elements. At that point, a new element is added to the computational grid. This allows avoiding an increase of the size of the problem at each time-step during sedimentation and, most notably, to deal with very small mesh elements.

Let $[0, t_{max}]$ be the time-interval of interest, which is uniformly discretized as $\{0 = t^0, t^1, \dots, t^M = t_{max}\}$, and Ω_0 the initial space domain, and let $h_{sea}(t)$ be the given paleobathymetry. We set the origin of the reference system at the sea level (Fig.1) and provide an initial mesh $Z^0 = \{z_{bot} = z_1, z_2, \dots, z_N = -h_{sea}\}$ with elements, $e_i^0 = [z_{i+1}, z_i]$, of uniform size $h = |z_{i+1} - z_i|$. Since we adopt a Lagrangian approach the element size changes during the basin evolution. As the strength of compaction is not uniform with depth, the deformed grid comprises elements of different size at each time step.

After the beginning of sedimentation at time t^1 , and depending on sedimentation velocity, U_{sed} , a certain number of time steps, say $K + 1$, is required before the newly deposited material attains a sufficient thickness which allows adding a new element to the computational mesh.

During these steps the grid is free to deform under the increasing sediment weight, yielding the updated configuration $Z^K = \{z_{bot}^K = z_1^K, z_2^K, \dots, z_N^K = z_{top}^K\}$ (Fig.1). At time t^{K+1} the grid is finally updated by adding a new element e_N on top: $Z^{K+1} = \{z_{bot}^{K+1} = z_1^{K+1}, \dots, z_N^{K+1}, z_{N+1}^{K+1} = z_{top}^{K+1}\}$.

3.2 A fixed point method for the basin evolution

For the numerical solution of the non-linear coupled system described in the previous sections we refer to the work of [26] related to three-dimensional basin modeling and based on an idea first presented in [13]. The methodology relies on a fixed point iteration which at each time step eventually leads to the values of the fluid pressure p^l , temperature T , porosity ϕ , volume fraction of quartz ϕ_Q , sedimentary loading S , solid and liquid phase velocity u^s and u^l and the updated grid configuration.

A relaxation-parameter, $\theta \in (0, 1]$, which is empirically adjusted according to the number of iterations needed to converge, is introduced to ensure the convergence of the fixed point method.

The iterative algorithm is formulated as follows. At each time step $t^K \rightarrow t^{K+1}$ set $p_{(0)}^l = (p^l)^K$, $\sigma_{(0)} = \sigma^K$, $T_{(0)} = T^K$, $\phi_{(0)} = \phi^K$, $(\phi_M)_{(0)} = \phi_M^K$, $(\phi_Q)_{(0)} = \phi_Q^K$, $u_{(0)}^s = (u^s)^K$, $Z_{(0)} = Z^K$ and $i = 0$. Then, for $i = 1, \dots$ we solve the equations for $S_{(i)}$, $p_{(i)}^l$, $T_{(i)}$, $\phi_{(i)}$, $(\phi_M)_{(i)}$, $(\phi_Q)_{(i)}$, $u_{(i)}^s$, $Z_{(i)}$ as follows [26]:

1. Estimate the sedimentary loading $S_{(i)}$ on the mesh $Z_{(i-1)}$ using porosity $\phi_{(i-1)}$ distribution at iteration $(i-1)$:

$$S_{(i)}(z_{j(i-1)}) = S(z_{top}) - \int_{z_{top}}^{z_{j(i-1)}} [\phi_{(i-1)}\rho^l + (1 - \phi_{(i-1)})\rho^s] g dz,$$

where $z_{j(i-1)}$ ($j = 1, \dots, N$) is the j -th node of the grid at iteration $(i-1)$, and the integral is approximated by the trapezoidal rule.

2. Compute a first value for the effective stress $\sigma_{(i)}^*$ using the new sedimentary loading value $S_{(i)}$ and the available pressure $p_{(i-1)}^l$, with a relaxed updating procedure

$$\sigma_{(i)}^* = \theta \left(S_{(i)} - p_{(i-1)}^l \right) + (1 - \theta)\sigma_{(i-1)}.$$

3. Using the computed stress and previous values for porosity and temperature, compute $\phi_{(i)}$ by calculating the variation due to mechanical compaction, $(\phi_M)_{(i)}$ and to the volume fraction of quartz $(\phi_Q)_{(i)}$ according to (8) (9) and (11), where time derivatives are approximated by finite differences. We apply the relaxation as

$$\phi_{(i)} = \theta\phi_{(i)} + (1 - \theta)\phi_{(i-1)}.$$

4. Solve the fluid and heat equations to obtain the pressure $p_{(i)}^l$ and the temperature $T_{(i)}$. The Darcy flow is also computed in this phase. For the sake of clarity, Section 3.3 reports the details of this step, which is the most complex and computationally expensive part of the procedure.
5. Recalculate the effective stress $\sigma_{(i)}$ with the new pressure

$$\sigma_{(i)} = S_{(i)} - p_{(i)}^l$$

6. Compute the grid velocity, $u_{(i)}^s$, using solid mass conservation at each node j ,

$$u_{(i)}^s(z_{j(i-1)}) = u^s(z_{top}) - \int_{z_{top}}^{z_{j(i-1)}} \frac{1}{1 - \phi_{(i)}} \frac{d(\phi_M)_{(i)}}{dt} dz.$$

7. Update the mesh $Z_{(i)}$ using the current velocity $u_{(i)}^s$

$$z_{j(i)} = z_j^K + u_{(i)}^s(z_{j(i-1)})(t^{K+1} - t^K).$$

8. Test for convergence and eventually update the relaxation parameter θ .

After the iterative cycle is completed we set $(p^l)^{K+1} = p^l_{(i)}$, $\sigma^{K+1} = \sigma_{(i)}$, $T^{K+1} = T_{(i)}$, $\phi^{K+1} = \phi_{(i)}$, $(\phi_M)^{K+1} = (\phi_M)_{(i)}$, $(\phi_Q)^{K+1} = (\phi_Q)_{(i)}$, $(u^s)^{K+1} = (u^s)_{(i)}$ and $Z^{K+1} = Z_{(i)}$. Convergence of the algorithm is tested on the mesh configuration. More precisely, the fixed point algorithm ends when the difference between two consecutive configurations of the domain, normalized by the elements size, is below a fixed tolerance.

3.3 The discretization fluid and heat equations

The elliptic problem associated with the fluid flow equation is solved at each step of the iteration procedure by a mixed finite-element method using $\mathbb{RT}_0 - \mathbb{P}_0$ finite elements [Brezzi]. This choice is justified by the robustness of the method within the context of highly heterogeneous media. Mixed finite-elements guarantee local mass conservation and provide an accurate fluid velocity field, at the expense of a slightly increased computational cost.

The fluid problem relies on equations (2) and (4). Considering pressure p^l as primal variable, the mixed strong formulation of the governing differential problem takes, for all $t \in (0, t_{max})$, the form

$$\left\{ \begin{array}{l} \tilde{k}(t)u(t) + \frac{\partial p^l}{\partial z}(t) = \rho^l g \quad \text{in } \Omega(t), \\ \frac{\partial u}{\partial z}(t) = f(t) \quad \text{in } \Omega(t) \\ u(t, z_{bot}(t)) = 0 \\ p(t, z_{top}(t)) = P, \end{array} \right.$$

where

$$\tilde{k}(t)(z) = \frac{\mu^l}{K(\phi(t, z))\rho^l}$$

and

$$f(t)(z) = f(t, z) = -\frac{\partial(\phi(t, z)\rho^l)}{\partial t} - \frac{\partial(\phi(t, z)\rho^l u^s(t, z))}{\partial z}.$$

Here, $u = \rho^l u^D$. This framework leads to a straightforward extension of the model in case of variable fluid density, $\rho^l = \rho^l(t, z)$.

The corresponding weak formulation can be expressed as follows. Given the initial datum $u(0) = u_0 \in V$ at each $t \in (0, t_{max})$ find $(p^l(t), u(t)) \in W \times V$ such that

$$\begin{aligned} \int_{\Omega(t)} \tilde{k}u(t)v - \int_{\Omega(t)} \frac{\partial v}{\partial z} p^l(t) &= \int_{\Omega(t)} \rho^l g v - P v(z_{top}), \\ \int_{\Omega(t)} \frac{\partial u}{\partial z}(t)w &= \int_{\Omega(t)} f(t), \end{aligned}$$

for all $(v, w) \in V \times W$, where $W = L^2(\Omega(t))$ and $V = \{v \in H^1(\Omega(t)) : v(z = z_{bot}) = 0\}$.

The problem is approximated by considering the domain $\Omega(t)$ formed by elements $e_j = e_j(t) = [z_j(t), z_{j+1}(t)]$, for $j = 1, \dots, N - 1$ and the $\mathbb{RT}_0 - \mathbb{P}_0$ finite element spaces $V_h = \{v \in V : v|_{e_j} \in \mathbb{RT}_0(e_j)\}$ and $W_h = \{w \in W : w|_{e_j} \in \mathbb{P}_0(e_j)\}$, leading to: find $(p_h^l, u_h) \in W_h \times V_h$ satisfying

$$\begin{aligned} \int_{\Omega(t)} \tilde{k} u_h \tau_i - \int_{\Omega(t)} \frac{\partial \tau_i}{\partial z} p_h &= \int_{\Omega(t)} \rho^l g \tau_i - P \tau_i(z_{top}) \\ \int_{\Omega(t)} \frac{\partial u_h}{\partial z} \varphi_j &= \int_{\Omega(t)} f \varphi_j \end{aligned}$$

for each basis function $\tau_i \in V_h$ and $\varphi_j \in W_h$. In this framework, velocity u is a nodal variable with N degrees of freedom while pore pressure p^l is constant on each mesh element. Note that N may change with time because sedimentation may require adding new elements to the computational mesh.

This choice of discrete spaces allows to compute the forcing term as

$$\begin{aligned} \int_{\Omega(t)} f \varphi_j &= - \int_{e_j(t)} \frac{\partial(\phi \rho^l)}{\partial t} - \int_{e_j(t)} \frac{\partial(\phi \rho^l u^s)}{\partial z} \\ &= - \frac{d}{dt} \int_{e_j(t)} \phi \rho^l, \end{aligned}$$

where Reynold's theorem has been employed in the second equality. The latter term can then be computed, at time step K , by a backward difference formula as

$$- \frac{\rho^l}{\Delta t} \left(\int_{e_j^{K+1}} \phi^{K+1} - \int_{e_j^K} \phi^K \right).$$

Note that ϕ^{K+1} is approximated by $\phi_{(i)}$, within the iterative procedure illustrated in Section 3.2.

Mixed finite elements have been adopted to solve the parabolic equation associated with the heat problem. In this case the temperature T is the primal variable, while the dual variable is

$$\sigma_T = K_T(T) \frac{\partial T}{\partial z} - bT.$$

To minimize computational cost the conductivity $K_T(T)$ is calculated using the value of temperature T computed at the previous iteration step, within the iterative procedure described in Section 3.2. This allows solving the heat equation as a linear problem in T , avoiding further fixed point iterations.

4 Global sensitivity analysis

Beside the modeling assumptions and the discretization errors associated with the selected numerical solution, the accuracy and reliability of computed predictions of a target quantity of interest, \mathcal{Q} (e.g., porosity at a desired depth and

Parameter	a_i	b_i
$\beta[\text{Pa}^{-1}]$	5×10^{-8}	7×10^{-8}
$a_q[\text{mol m}^{-2} \text{ s}^{-1}]$	0.40×10^{-18}	3.56×10^{-18}
$b_q [\text{C}^{-1}]$	0.0213	0.0227
$T_c [\text{C}]$	70	90
$h_{sea}[\text{m}]$	450	550
$k_1 [-]$	14.07	14.22
$k_2 [-]$	1.35	2.38

Table 1: List of the selected uncertain parameters. Each parameter is modeled as a uniform random variable ranging between a_i and b_i .

time), depend also on model parameters. Some of these parameters are virtually impossible to assess (e.g., all parameters linked with the initial conditions of the problem), while knowledge of others is plagued by uncertainty due to scarcity of direct measurements at appropriate space-time resolution scales.

Assessment of how the uncertainty on the unknown parameters propagates to the output of the model is therefore of utmost relevance. This analysis is typically known as “uncertainty quantification” or “sensitivity analysis” and aims at quantifying the uncertainty associated with the model output \mathcal{Q} (e.g., in terms of second-order statistical moments) and identifying the relative contribution of the unknown parameters to this uncertainty.

Amongst the different available approaches, e.g., perturbative methods and Taylor expansions [3, 21], evidence theory [15, 35], and fuzzy sets theory [20, 22], in this work we focus on a probabilistic approach to the uncertainty quantification problem.

We consider the uncertain parameters as random variables, collected as the (random) component of vector $\mathbf{x} = (x_1, x_2, \dots, x_N)^T$. A quantity of interest \mathcal{Q} , which is the outcome of our computational model for each realization of the random vector \mathbf{x} , is denoted as a space-time function $\mathcal{Q} = \mathcal{Q}(\mathbf{x})$.

The set of parameters that we consider as uncertain is introduced in Section 4.1. Section 4.2 illustrates the proposed sensitivity analysis procedure, which is based on the use of the Sobol indices and their computation through the generalized PCE (GPCE) of \mathcal{Q} . Finally, Section 4.3 and 4.4 present a methodology to compute the GPCE using the so-called sparse grid operators (see, e.g., [14]).

4.1 Choice of the random model parameters

Table 1 lists the set of seven parameters which are considered as uncertain for our illustrative example.

Our choice includes the parameters affecting the compaction process and the

characterization of the hydraulic conductivity of the sandstone. The parameters selected are: β , the two parameters, a_q and b_q , driving the quartz cementation rate kinetics (1), the activation temperature of the geochemical process T_c , the depth of the sea imposed at the top of the basin, h_{sea} , and the two parameters k_1 , k_2 appearing in (3).

An uncertainty range is assigned to each of these parameters, i.e., $x_i \in \Gamma_i = [a_i, b_i]$. The uncertainty associated with β is consistent with the sensitivity study presented in [24]. The estimation of the bounds of the intervals associated with the quartz cementation rate parameters is based on the calibration data reported in [41]. The reference value of T_c is taken as 80 °C and we assume an uncertainty of ± 10 °C, consistently with the analysis of [24]. For our illustration purposes, we assume an uncertainty of about $\pm 10\%$ associated with a reference value of $h_{sea} = 500\text{m}$. The range of variability of k_1 and k_2 has been estimated after the sandstone permeability measurements reported in [44].

In the absence of an a-priori knowledge on the probability distribution of these parameters, we assume each x_i to be uniformly distributed within its variation interval Γ_i . We denote with Γ the hypercube $\Gamma = \Gamma_1 \times \Gamma_2 \dots \times \Gamma_N$, so that each realization $\mathbf{x} \in \Gamma$. We further assume that all x_i are statistically independent. As a consequence, the joint probability density function of \mathbf{x} over Γ is the product of uniform probability density functions along each direction

$$\rho_{\Gamma}(\mathbf{x}) = \prod_{i=1}^N \rho_{\Gamma_i}(x_i) = \prod_{i=1}^N \frac{1}{b_i - a_i}. \quad (14)$$

All the remaining parameters introduced in the mathematical model are considered to be fixed in the context of our example. Our choice is indeed arbitrary, as virtually all parameters are affected by uncertainty, and aims at demonstrating the main features of the proposed technique by including some of the key parameters affecting the compaction process and the ensuing feedback on porosity, pressure and temperature distributions. The extension of the methodology to include an enlarged set of uncertain parameters is straightforward.

4.2 Sobol indices

We perform a global sensitivity analysis of the problem by evaluating the so-called Sobol indices [37, 2, 34, 39]. These indices provide a complete description of the decomposition of the total variance of the quantity of interest into (a) the effects of each random variable x_i and (b) mixed/joint effects of different variables $x_{i_1}x_{i_2} \dots x_{i_s}$ (see e.g. [2] for a discussion in the context of classical ANOVA techniques). With respect to other strategies (e.g., the one factor at a time approach), Sobol indices provide a general result as they do not assume any linearity in the considered model (see e.g. [34]).

Following [37, 25, 39], we first introduce the Hoeffding/Sobol decomposition

of a function f depending on N independent random variables,

$$\begin{aligned}
f(\mathbf{x}) &= f_0 + \sum_{i=1}^N f_i(x_i) + \sum_{i,j=1}^N f_{ij}(x_i, x_j) + \dots + f_{1,2,\dots,N}(x_1, x_2, \dots, x_N), \quad (15) \\
f_0 &= \int_{\Gamma} f(\mathbf{x}) \rho_{\Gamma}(\mathbf{x}) d\mathbf{x}, \\
f_i(x_i) &= \int_{\Gamma_{\sim i}} f(\mathbf{x}) \rho_{\Gamma_{\sim i}}(\mathbf{x}) d\mathbf{x}_{\sim i} - f_0 \\
f_{i,j}(x_i, x_j) &= \int_{\Gamma_{\sim i,j}} f(\mathbf{x}) \rho_{\Gamma_{\sim i,j}}(\mathbf{x}) d\mathbf{x}_{\sim i,j} - f_i(x_i) - f_j(x_j) - f_0,
\end{aligned}$$

and so on, where e.g. $\int_{\Gamma_{\sim i}} f(\mathbf{x}) \rho_{\Gamma_{\sim i}}(\mathbf{x}) d\mathbf{x}_{\sim i}$ represents integration of f over the space of all variables (excluding the i -th variable) against the product of the probability density functions of $i - 1$ variables, ρ_{Γ_k} . Note that all the terms in (15) are orthogonal, i.e.,

$$\int_{\Gamma} f_{i_1, i_2, \dots, i_s} f_{j_1, j_2, \dots, j_r} \rho_{\Gamma}(\mathbf{x}) d\mathbf{x} = 0,$$

for $\{i_1, i_2, \dots, i_s\} \neq \{j_1, j_2, \dots, j_r\}$. Thus, denoting with V_f the variance of f , one obtains

$$V_f = \int_{\Gamma} f(\mathbf{x})^2 \rho_{\Gamma}(\mathbf{x}) d\mathbf{x} - f_0^2,$$

and the Sobol index S_{i_1, i_2, \dots, i_s} corresponding to the mixed effect of $x_{i_1} x_{i_2} \dots x_{i_s}$ can be computed by integrating the summands of (15) and dividing by V_f

$$S_{i_1, \dots, i_s} = \frac{1}{V_f} \int_{\Gamma_{i_1, \dots, i_s}} f_{i_1, \dots, i_s}^2(x_{i_1} \dots x_{i_s}) \rho_{\Gamma_{i_1, \dots, i_s}}(\mathbf{x}) dx_{i_1} \dots dx_{i_s}$$

where $\Gamma_{i_1, \dots, i_s} = \Gamma_{i_1} \times \dots \times \Gamma_{i_s}$ and $\rho_{\Gamma_{i_1, \dots, i_s}}(\mathbf{x})$ is the corresponding probability measure. Note that Sobol indices sum up to unity. The total variability due to the i -th random parameter is then the sum over all mixed effects including x_i

$$S_i^T = \sum_{\mathcal{S}} S_{i_1, i_2, \dots, i_s}, \quad (16)$$

\mathcal{S} denoting the subset of all indices including i .

4.3 Generalized polynomial chaos expansion

To compute the Sobol indices defined in (16), high-dimensional quadrature rules are typically needed. To this purpose, one could employ simple Monte Carlo quadrature schemes. However, these can be extremely computationally intensive. Indeed, the convergence rate of these schemes is only $1/\sqrt{M}$, M being the number of points sampled from Γ . The generalized polynomial chaos expansion

[46, 18, 48] of the quantity of interest $\mathcal{Q}(\mathbf{x})$ can then be introduced to reduce the computational burden associated with the evaluation of the Sobol indices, as shown in [25] and [39].

Given a function f depending on N random variables, $f = f(\mathbf{x})$, the generalized polynomial chaos expansion of f is the spectral expansion of f over a set of polynomials $\psi_{\Gamma,i}(\mathbf{x})$ that are orthogonal with respect to the probability measure¹ of Γ . In our case we can use the multidimensional Legendre polynomials (see e.g. [17]), which are orthonormal with respect to the uniform probability density function (14). Such polynomials are built as products of one-dimensional Legendre polynomials in terms of each random variable considered. It is therefore useful to introduce the following notation

$$L_{\mathbf{p}}(\mathbf{x}) = \prod_{n=1}^N L_{n,p_n}(x_n),$$

where $L_{\mathbf{p}}(\mathbf{x})$ is a multidimensional Legendre polynomial and $L_{n,p_n}(x_n)$ is the p_n -th Legendre polynomial (see, e.g., [17]). With this notation, the generalized polynomial chaos expansion (GPCE) of f reads

$$f(\mathbf{x}) = \sum_{\mathbf{p} \in \mathbb{N}^N} \alpha_{\mathbf{p}} L_{\mathbf{p}}(\mathbf{x}), \quad \alpha_{\mathbf{p}} = \int_{\Gamma} f(\mathbf{x}) L_{\mathbf{p}}(\mathbf{x}) \rho_{\Gamma}(\mathbf{x}) d\mathbf{x}. \quad (17)$$

Note that whenever \mathbf{p} is such that $p_n = 0$, then $L_{\mathbf{p}}(\mathbf{x})$ is independent of x_n because $L_0(x_n) = 1$, see [17]. As a consequence, one can reorder the expansion (17) so that it is equivalent to (15), and derive an equivalence between the Sobol indices (16) and the coefficients $\alpha_{\mathbf{p}}$ of the GPCE expansion of $f(\mathbf{x})$

$$f(\mathbf{x}) = \alpha_0 + \sum_{i=1}^N \sum_{\mathbf{p} \in \mathcal{P}_i} \alpha_{\mathbf{p}} L_{\mathbf{p}}(\mathbf{x}) + \sum_{i=1}^N \sum_{j=i}^N \sum_{\mathbf{p} \in \mathcal{P}_{i,j}} \alpha_{\mathbf{p}} L_{\mathbf{p}}(\mathbf{x}) + \dots, \quad (18)$$

where \mathcal{P}_i contains all the indices such that only the i -th component is different from 0, i.e., $\mathcal{P}_i = \{\mathbf{p} \in \mathbb{N}^N : p_i \neq 0, p_k = 0 \text{ for } k \neq i\}$, and so on.

Therefore, (18) and the orthonormality of the Legendre polynomials leads to

¹a family of polynomials $\psi_{\Gamma,i}(\mathbf{x})$ is said to be orthogonal with respect to the probability measure $\rho_{\Gamma}(\mathbf{x})$ if

$$\int_{\Gamma} \psi_i(\mathbf{x}) \psi_j(\mathbf{x}) \rho_{\Gamma}(\mathbf{x}) d\mathbf{x} \neq 0 \text{ only if } i = j$$

The polynomials are said to be orthonormal if

$$\int_{\Gamma} \psi_i^2(\mathbf{x}) \rho_{\Gamma}(\mathbf{x}) d\mathbf{x} = 1.$$

the following equivalences between GPCE coefficients and Sobol indices

$$S_{i_1, i_2, \dots, i_s} = \sum_{\mathbf{p} \in \mathcal{P}_{i_1, i_2, \dots, i_s}} \frac{\alpha_{\mathbf{p}}^2}{V_f}, \quad V_f = \sum_{\mathbf{p} \in \mathbb{N}^N} \alpha_{\mathbf{p}}^2 \quad (19)$$

$$S_i^T = \sum_{i_1, i_2, \dots, i_s \in \mathcal{R}} S_{i_1, i_2, \dots, i_s} \quad (20)$$

where the set \mathcal{R} contains all the mixed effects that include the random variable x_i .

Note that (19) and (20) include summations over a countable infinite number of terms. A workable approximation is usually obtained upon truncating the GPCE (17) to the set \mathbb{P}_w of polynomials whose total degree does not exceed $w \in \mathbb{N}$, i.e. upon restricting (17)-(20) to the set

$$TD(w) = \{\mathbf{p} \in \mathbb{N}^N : \sum_i p_i \leq w\}. \quad (21)$$

In other words, one computes the Sobol indices of the approximation of f in \mathbb{P}_w rather than of f itself. The accuracy of the approximation increases as $w \rightarrow \infty$. The reader is referred to [4, 6] and references therein for other possible truncation schemes.

4.4 Sparse grid computation of GPCE

Equation (19) provides an expedient way to compute the Sobol indices once the GPCE (18) for $f(\mathbf{x})$ has been determined. However, computing the coefficients $\alpha_{\mathbf{p}}$ on the basis of (17) would still require the evaluation of a number of high-dimensional integrals. To circumvent this problem we introduce the construction of the sparse grid polynomial interpolant. The GPCE of the sparse grid approximation allows then direct calculation of the Sobol indices.

To derive the sparse grid interpolant we first introduce some notation. Given $l_n \in \mathbb{N}$, let

$$\mathcal{H}_n^{l_n} = \{x_{n,1}, x_{n,2}, \dots, x_{n,l_n}\} \subset \Gamma_i \quad (22)$$

be a set of l_n interpolation points that provides an accurate interpolation with respect to the uniform probability measure $\rho_{\Gamma_i}(x_i)$, e.g., the Gauss–Legendre points [31], or the Clenshaw–Curtis points [40].

Next, let $\mathcal{L}_k(x_n)$, $k = 1, \dots, l_n$ be the set of Lagrangian polynomials over the set of points $\mathcal{H}_n^{l_n}$. These are polynomials of degree $l_n - 1$, such that their value is either 1 or 0 at the selected interpolation points,

$$\mathcal{L}_k(x_{n,j}) = \begin{cases} 1 & \text{if } x_{n,j} = x_{n,k}, \\ 0 & \text{if } x_{n,j} \neq x_{n,k}. \end{cases}$$

Taking the Cartesian product of the sets $\mathcal{H}_n^{l_n}$, we can build a tensor interpolation grid with M_1 points, $M_1 = l_1 \times l_2 \times \dots \times l_N$. We denote such tensorized grid as

\mathcal{H}_1 , where

$$\mathcal{H}_1 = \mathcal{H}_1^{l_1} \times \mathcal{H}_2^{l_2} \times \dots \times \mathcal{H}_N^{l_N}.$$

Each point x of the grid can also be addressed by a multi-index notation $\mathbf{i} \in \mathbb{N}^N$, e.g. $\mathbf{x}_i = (x_{1,i_1}, \dots, x_{N,i_N})$. One can then introduce the set of tensorized Lagrangian polynomials over \mathcal{H}_1 ,

$$\mathcal{L}_{\mathbf{k}}(\mathbf{x}) = \prod_{n=1}^N \mathcal{L}_{k_n}(x_n)$$

with the property $\mathcal{L}_{\mathbf{k}}(\mathbf{x}_j) = 1$ if $\mathbf{x}_j = \mathbf{x}_{\mathbf{k}}$ and 0 otherwise. The tensor grid interpolant for f is then defined as

$$f_{TG,1}(\mathbf{x}) = \sum_{\mathbf{x}_i \in \mathcal{H}_1} f(\mathbf{x}_i) \mathcal{L}_i(\mathbf{x}). \quad (23)$$

This can be rewritten in terms of tensorized interpolant operators. Denoting by $\mathcal{U}_n^{l_n}$ the operator that interpolates a function of x_n over the set of points, i.e., $\mathcal{H}_n^{l_n}$,

$$\mathcal{U}_n^{l_n}[f](x_n) = \sum_{k=1}^{l_n} f(x_{n,k}) \mathcal{L}_k(x_n),$$

one obtains

$$f_{TG,1}(\mathbf{x}) = \bigotimes_{n=1}^N \mathcal{U}_n^{l_n}[f](\mathbf{x}).$$

Note that the tensor grid is associated with the subscript $\mathbf{1}$, that specifies the interpolation level along each direction in the random parameters space.

Building such tensor interpolant requires evaluating f at M_1 points. An appropriate choice of the interpolation points along each direction allows fast convergence of the tensor interpolant to the the original function. On the other hand, building such an approximation can be excessively expensive, because M_1 could be very large. For example, using only 5 points along each direction in our example would entail using a total of $M_1 = 5^N = 5^8 = 390,625$ points.

The sparse grid is a way of reducing the computational cost of building tensor grids interpolants, while retaining good approximation properties. This can be achieved upon building the interpolant as a particular linear combination of tensor grids, where each one of these contains only a limited number of points. To this purpose, let us further introduce the detail operator along each direction as the difference between two consecutive interpolation levels

$$\Delta_n^{l_n}[f] = \mathcal{U}_n^{(l_n)}[f] - \mathcal{U}_n^{(l_n-1)}[f]. \quad (24)$$

Tensorizing detail operators along each direction leads to the so-called hierarchical surplus operator

$$\Delta^{\mathbf{1}}[f] = \bigotimes_{n=1}^N \Delta_n^{l_n}[f]. \quad (25)$$

Note that hierarchical surpluses are also indexed by a multi-index notation, $\mathbf{l} \in \mathbb{N}^N$. One can then define the sparse grid approximation of f [36, 5, 12] as a suitable sum of hierarchical surpluses

$$f_{SG} = \sum_{\mathbf{l} \in \mathcal{I}} \Delta^{\mathbf{l}}[f], \quad (26)$$

where $\mathcal{I} \subset \mathbb{N}^N$ is a set of multi-indices that selects the hierarchical surpluses included in the sparse grid, and hence the set of tensor grids that form the sparse grid. Indeed, employing the definitions (24) and (25) into (26) allows recasting the sparse grid approximation operator as a linear combination of tensor grid interpolants as

$$f_{SG}(\mathbf{x}) = \sum_{\mathbf{l} \in \mathcal{I}} c_{\mathbf{l}} f_{TG, \mathbf{l}}(\mathbf{x}) = \sum_{\mathbf{l} \in \mathcal{I}} c_{\mathbf{l}} \bigotimes_{n=1}^N \mathcal{U}_n^{l_n}[f](\mathbf{x}), \quad (27)$$

with suitable computable coefficients $c_{\mathbf{l}}$ (see, e.g., [5, 6]). The set of all points required by the sparse grid is the union of the points of each tensor grid that forms the sparse grid

$$\mathcal{G} = \bigcup_{\mathbf{l} \in \mathcal{I}, c_{\mathbf{l}} \neq 0} \mathcal{H}_{\mathbf{l}}. \quad (28)$$

The set \mathcal{I} needs to be chosen properly, to retain good approximations with a small number of function evaluations. The underlying idea that should govern the process of selection is that whenever one allocates many points along one direction, i.e. a fine detail operator is employed in one direction, there is no need to adopt a large number of points along the other directions, because one can expect the high details to be small and their product to be negligible.

A simple choice of \mathcal{I} that turns out to be quite effective in discarding the irrelevant hierarchical surpluses is

$$\mathcal{I} = \left\{ \mathbf{l} \in \mathbb{N}^N : \sum_{n=1}^N l_n - 1 \leq w, w \in \mathbb{N} \right\}. \quad (29)$$

A key observation is that the sparse grid approximation resulting from (29) belongs to the polynomial space \mathbb{P}_w introduced in (21) (see [4] for a proof). As a consequence, it is possible to convert the sparse grid approximation (26) into its equivalent GPCE representation (18), and then compute the Sobol indices avoiding numerical quadratures. The reader is referred to [4, 6] for an analysis on the choice of the set \mathcal{I} , and for the links between the GPCE expansion and the sparse grid approximation.

The conversion from sparse grid to GPCE expansion relies on the property that a sparse grid is composed by a linear combination of tensor grid Lagrangian interpolants (23), and is based on two steps: (a) each tensor Lagrangian interpolant is reformulated in terms of Legendre polynomials; and (b) the Legendre polynomials associated with different tensor grids are summed.

With reference to the first step, consider the \mathbf{l} -th tensor grid, \mathcal{H}_1 . The corresponding Lagrangian interpolant $f_{TG,1}(\mathbf{x})$ in (23) is a sum of products of one-dimensional Lagrange polynomials, respectively on l_1, l_2, \dots, l_N points. It can then be formulated as a linear combination of all the Legendre polynomials whose maximum degree along direction n does not exceed $l_n - 1$, that is

$$f_{TG,1}(\mathbf{x}) = \sum_{\mathbf{p} \in \mathcal{C}_1} \beta_{\mathbf{p}} L_{\mathbf{p}}(\mathbf{x}),$$

$$\mathcal{C}_1 = \{\mathbf{p} \in \mathbb{N}^N : p_n \leq l_n - 1, n = 1, \dots, N\}.$$

The coefficients $\beta_{\mathbf{p}}$ of this linear expansion can be easily calculated by solving the linear system

$$\sum_{\mathbf{p} \in \mathcal{C}_1} \beta_{\mathbf{p}} L_{\mathbf{p}}(\mathbf{x}_j) = f_{TG,1}(\mathbf{x}_j), \quad \forall \mathbf{x}_j \in \mathcal{H}_1. \quad (30)$$

In essence, converting the sparse grid into a GPCE entails solving as many systems (30) as the number of tensor grids in the sparse grid, and then collecting coefficients $\beta_{\mathbf{p}}$ for the same \mathbf{p} associated with different tensor grids. Note that the matrix of this linear system is not ill-conditioned, due to the properties of the selected interpolation points. In particular, using Gauss-Legendre points renders an orthogonal matrix. This implies that the conversion algorithm will be very efficient, since no linear system has to be solved. This is not true for the above-mentioned Clenshaw–Curtis points. In this case, however, the sparse grid construction can take advantage of the fact that the interpolation points used are nested. FFT techniques can be used to solve efficiently the system and to compute the coefficients $L_{\mathbf{p}}(\mathbf{x}_j)$.

Finally, we remark that it is straightforward to build a sparse grid quadrature scheme starting from (27–28), and to approximate the statistical moments of f once its sparse grid approximation has been computed. Indeed, suppose that the interpolation points (22) along the n -th direction are now used as quadrature points with associated weights $\gamma_{n,1}, \gamma_{n,2}, \dots, \gamma_{n,l_n}$, i.e.

$$\int_{\Gamma_n} g(x_n) \rho_{\Gamma_n}(x_n) dx_n \approx \sum_{i=1}^{l_n} g(x_{n,i}) \gamma_{n,i}.$$

The sparse grid quadrature rule then naturally descends from (27) and reads

$$\int_{\Gamma} f(\mathbf{x}) \rho_{\Gamma}(\mathbf{x}) d\mathbf{x} \approx \sum_{\mathbf{l} \in \mathcal{I}} c_{\mathbf{l}} \sum_{\mathbf{x}_i \in \mathcal{H}_1} f(\mathbf{x}_i) \lambda_i, \quad \lambda_i = \prod_{n=1}^N \gamma_{n,i_n}.$$

5 Results

We illustrate here the results of the sensitivity analysis through an example. The uncertain parameters space is presented in Table 1. We consider a total

sedimentation time of 200 Ma and a fixed sedimentation rate of 30 m/Ma. The temperature is set to 295K at the top of the basin, whereas a geothermal gradient of 0.03K/m is imposed at the bottom. No fluid flow conditions ($u^l = 0$) are imposed at the bottom. A pressure value corresponding to the hydrostatic pressure of the overlying sea depth is assigned at the top. The basin is considered as homogeneous and fully composed by quartz material. This implies that the quartz can precipitate and completely fill the pore space.

5.1 Comparison with a standard Monte Carlo sampling

We start by comparing the approximation of statistical moments obtained through the sparse grid quadrature against those obtained through a standard Monte Carlo analysis of the problem to assess the reliability of the sparse grid technique. The uncertainty on the mean values computed making use of the Monte Carlo analysis can be evaluated through the standard deviation of the predictor, defined as $\sigma(\mu(s_i)) = \sigma(s_i)/\sqrt{M}$, where $\mu(s_i)$ and $\sigma(s_i)$ are the mean and the standard deviation calculated on the basis of M realizations of the generic variable s_i . The analysis illustrated here is based on $M = 10^5$. Figure 2 depicts the evolution of the coefficient of variation associated with the Monte Carlo prediction standard deviation defined above, i.e., $CV(\mu(s_i)) = \sigma(\mu(s_i))/\mu(s_i)$ with $s_i = \phi, T, p$, for four different times. For any considered time the distribution of the statistical moments of the sample along the vertical direction can be obtained. We select here the largest value of $CV(\mu(s_i))$ for each of the observation times considered. The largest uncertainties are associated with the average porosity ϕ , with $CV(\mu(\phi))$ attaining values of about 1%. The coefficients of variation of mean pressure and temperature are always smaller than 10^{-4} .

Figure 3 shows L^2 -norm in space of the relative error between the mean and the variance computed with the sparse grid and the standard Monte Carlo simulation of the system and corresponding to the same time frames considered in Figure 2. The sparse grid is composed by 589 collocation points in the parameter space. The mean porosity error is comprised between 10^{-3} and 10^{-6} . The errors are smaller than the corresponding uncertainty, shown in Figure 2. Pressure and temperature relative errors are generally smaller than 10^{-4} (Figure 3 (a)). The variances of the variables exhibit an error of about 1% with respect to a standard Monte Carlo analysis, providing an acceptable accuracy (Figure 3 (b)). In summary, our results indicate that the sparse grid computation provides reliable results, greatly reducing the number of collocation points with respect to the reference Monte Carlo analysis and can be profitably employed for the derivation of a surrogate model in terms of a GPCE of the solution.

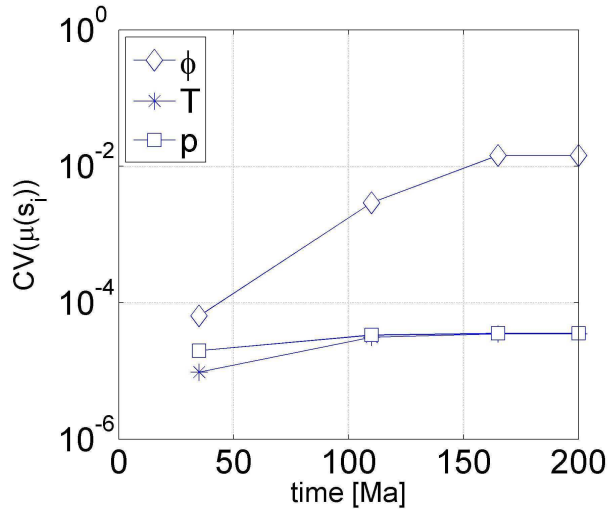


Figure 2: Relative uncertainty of the Monte Carlo sampling-based mean of ϕ , T and p .

5.2 Sensitivity and uncertainty propagation analysis

We devote this section to the analysis of the results of the sensitivity analysis carried out through the sparse grid method. For illustrative purposes, we focus on the analysis of the last time step of the simulation.

Figures 4-6 show the distribution of the main state variables characterizing the system at the final computation time, the associated uncertainty and the related source. Figure 4 (a) shows the vertical distribution of porosity and the related standard deviation. Three regions can be distinguished. In the upper zone of the basin the porosity change is driven by pure mechanical compaction. Quartz precipitation starts around $z = -2000\text{m}$ and the rate of porosity reduction increases with burial depth. This difference between the two zones is documented by the distribution of the Sobol indices depicted in Figure 4 (b). In this example we choose to examine the behavior of the total Sobol indices, i.e., the sum of all the indices involving each of the considered parameters. For the upper layer most of the uncertainty is due to the boundary data h_{sea} (defined in Figure 1). The influence of this parameter sharply decreases for $z < 2000\text{m}$. The β parameter of mechanical compaction has a dominant influence for $-1000 > z > -1800\text{m}$. The related Sobol index then decreases for $-1800 > z > -3000\text{m}$. A localized effect of the activation temperature of the quartz cementation process T_c can be observed in this region. The parameters of the quartz precipitation model largely influence the uncertainty of the output porosity distribution for $z < -2200\text{m}$, where, in particular, the total Sobol index associated with a_q approaches unity. The effect of mechanical compaction is greatly reduced but not completely absent (the related index is approximately

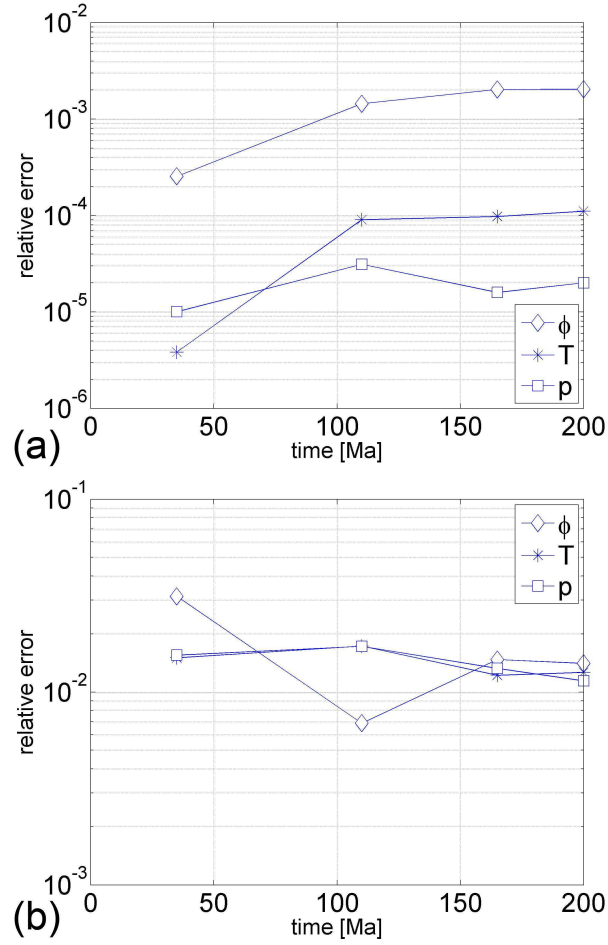


Figure 3: Relative L^2 -norm error of the (a) mean and (b) variance of ϕ , T and p computed by means of sparse grid method with respect to a standard Monte Carlo analysis.

0.05 for $-3000 > z > -4000$). In the deepest layers of the basin ($z < -4000$ m) the pore space completely is filled with quartz due to geochemical compaction and the porosity tends to vanish. In this region the calculated Sobol indices are not significant due to very small porosity values and exhibit an oscillatory behavior. This feature of the solution is induced by the choice of a homogeneous material in our example, where quartz precipitation is allowed everywhere and neglects the occurrence of grain coating effects.

Figure 5 reports the vertical distribution of mean temperature and the related indices. The temperature increases with depth, as expected. We observe a joint effect of the mechanical and geochemical compaction processes on the temperature distribution. As in the case of porosity, the overlying sea depth, h_{sea} , and the mechanical compaction coefficient influence the uncertainty of the results in

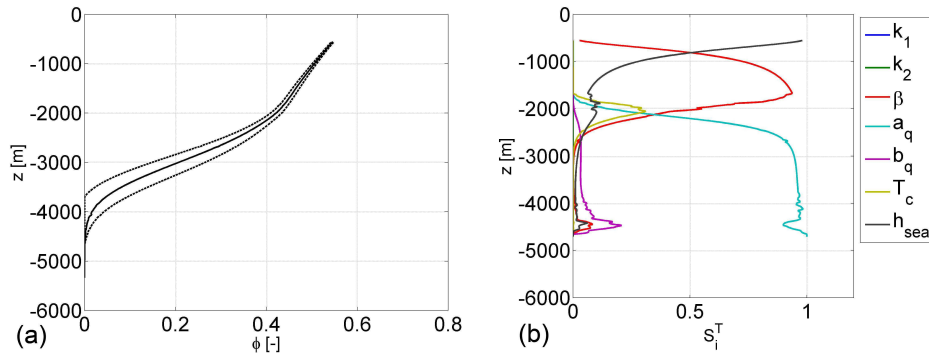


Figure 4: Final snapshot of the computed vertical distribution of mean porosity and related uncertainty (a) and Sobol indices (b).

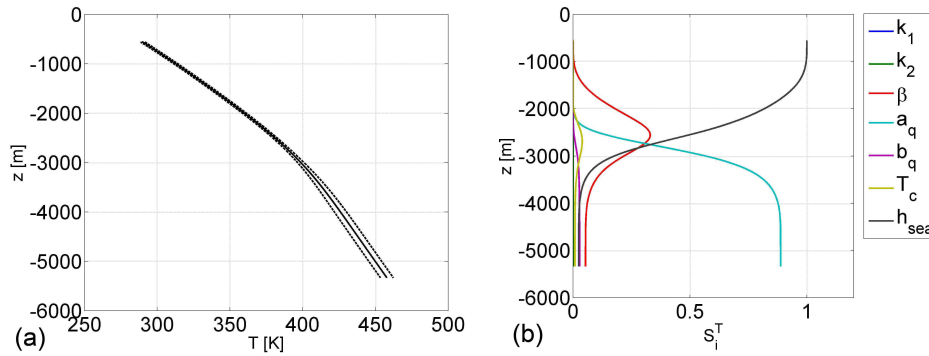


Figure 5: Final snapshot of the computed vertical distribution of mean temperature and related uncertainty (left) and Sobol indices (right).

the most superficial layers ($z > 2000\text{m}$). Notice that β has a smaller influence on temperature than on porosity (in this case the related index never exceeds 0.4). On the other hand, the influence of h_{sea} is larger on temperature than on porosity. Geochemical parameters start playing an important role for the deepest locations. We observe that the gradient of temperature smoothly changes in the region where geochemical compaction is active ($-2000 > z > -4000\text{m}$). These results suggest that all the variability of the temperature distribution is induced by the difference of thermal diffusivities associated with the solid and the liquid phases. Hence, it is intrinsically linked to the porosity field. Fluid mass transfer plays a negligible role in the thermal problem, i.e., heat exchange associated with the movement of fluid in the pore space is not relevant. The influence of T_c is less evident on temperature than on porosity (compare Figure 5 (b) with Figure 4 (b)). The Sobol indices related to the temperature field vary more smoothly in space than those associated with the porosity. This behavior may be ascribed to the format of the underlying differential problem. The

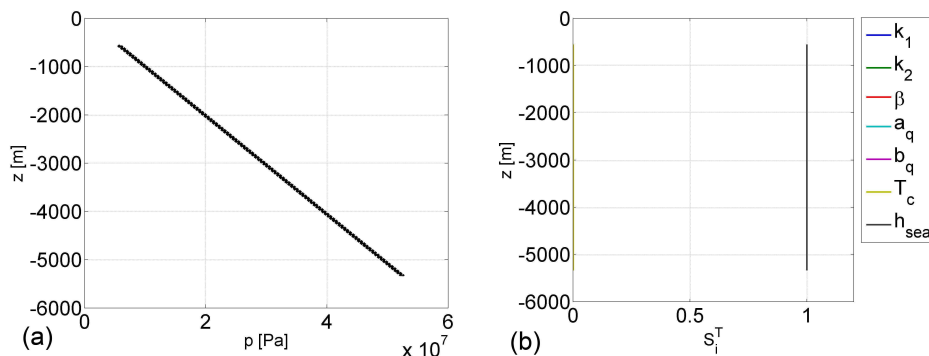


Figure 6: Final snapshot of the computed vertical distribution of mean pressure and related uncertainty (left) and Sobol indices (right).

vertical distribution of pressure and the Sobol indices are shown in Figure 6. The pressure distribution appears to vary essentially linearly with depth. The uncertainty in fluid pressure distribution is completely associated with h_{sea} , and no significant feedback of the geochemical compaction process on pressure is noted. Hence, no over pressure phenomena due to geochemical compaction are detected in the analyzed configuration. This particular result is likely related to the adoption of a homogeneous material.

Figure 7 depicts the vertical distribution of the calculated coefficients of variation of ϕ (CV_ϕ), T (CV_T) and p (CV_p) at the final simulation time. CV_ϕ smoothly increases up to 2×10^{-2} for $z > -2000$ m. It then sharply increases up to 1 where the geochemical processes are active. The values of CV_ϕ for $z < -4000$ m are not significant, as the mean porosity tends to vanish in this region. CV_T is approximately 10^{-3} at the top of the basin where the uncertainty due to h_{sea} is largest. It slightly decreases up to a depth $z \approx -2500$ m. As geochemical compaction influence starts to be relevant, CV_T increases up to 2 % for the deepest layers. CV_p continuously decreases with depth and is of the order of 10^{-2} on the whole domain. Consistently with what noted for the corresponding Sobol indices, we do not observe any change in the trend of CV_p due to the activation of geochemical compaction process.

We exploited the GPCE based reduced model of the problem solution to perform a Monte Carlo analysis based on 2.5×10^5 evaluations of the GPCE of the solution at the final time in the selected parameters space. This analysis can be performed with a very low computational cost, as the surrogate model is written in terms of an analytical (polynomial) formulation. The results can be used to evaluate the probability density function (pdf) of each quantity at any point along the vertical direction. In Figure 8 we focus our analysis on three selected locations: S0, located at $z = -1000$ m, in the region where compaction is purely mechanical; S1 and S2 respectively located at $z = -2000$ m and $z = -3000$ m, where quartz cementation is active. All the pdfs presented

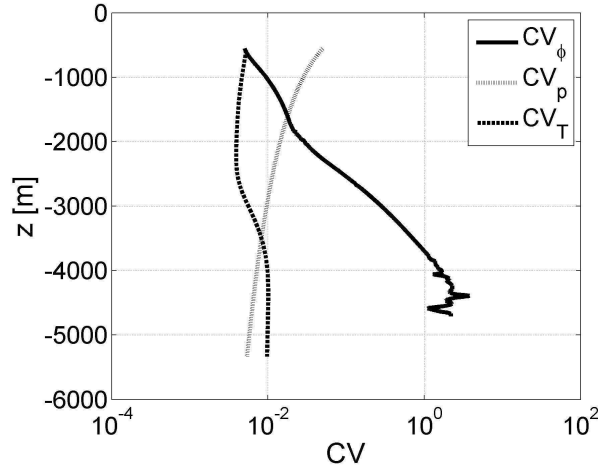


Figure 7: Vertical distribution of the coefficients of variation at the final computation time.

are centered around the mean value. The variability of the porosity increases with depth, and consequently, the associated pdf shows an increasing dispersion with around its the mean value (see Figure 8 (a)). The pdf is initially symmetric (at location S0), and then becomes progressively asymmetric, displaying a long tail towards the largest porosity values. Figure 8 (b) shows the evolution of the pdf of temperature with depth. The temperature pdf appears very similar to a uniform distribution at location S0: the uncertainty of the results is completely due to the variability of h_{sea} (see Figure 5 (b)). The asymmetry detected for porosity appears only at location S2, whereas the distribution is still symmetric at S1. Note that the geochemical compaction parameters start influencing the temperature field only for $z > 2000\text{m}$, as indicated by the related indices in Figure 5 (b). These results suggest that the asymmetry of the pdfs may be linked to the influence of the geochemical model parameters. On the other hand the pdf of pressure is very similar to a uniform distribution (with almost constant dispersion) at all the locations selected (see Figure 8 (c)). This result is consistent with the observation that the pressure uncertainty is entirely due to the paleobathymetry h_{sea} , as shown in Figure 6 (b).

6 Conclusions

Our work leads to the following major conclusions.

- The nonlinear propagation of the uncertainty on the parameters and boundary conditions during the geochemical and mechanical evolution of a basin-scale sedimentation process has been analyzed through a generalized Polynomial Chaos Expansion (GPCE) of the solution of the mathematical

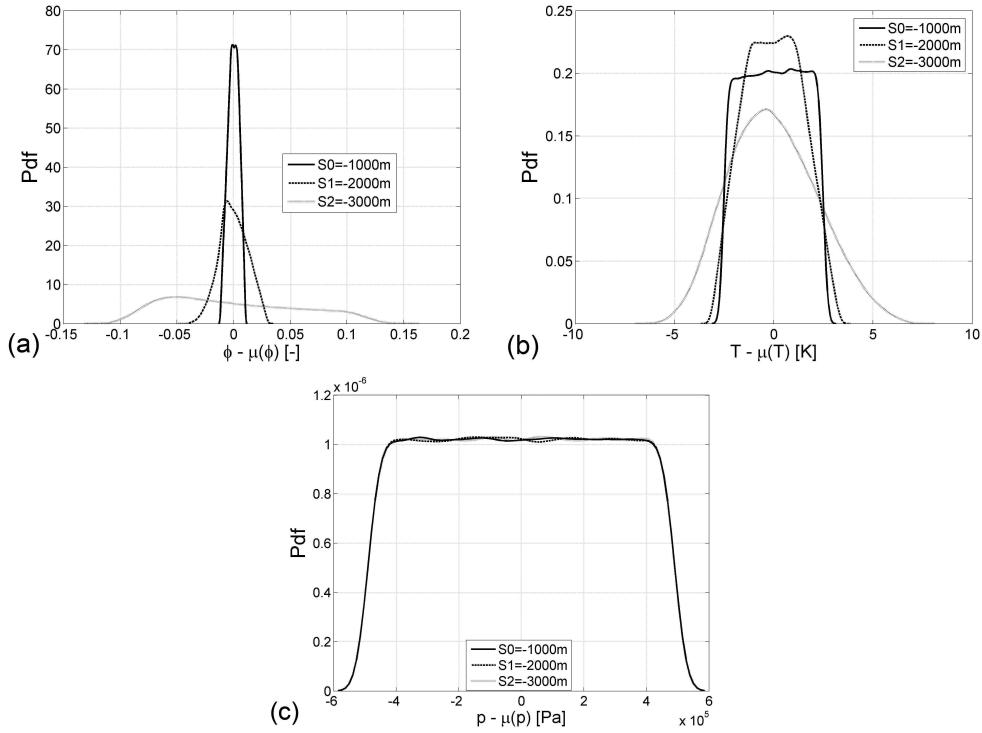


Figure 8: Probability density distributions of porosity (a), temperature (b) and pressure (c) evaluated at the final time at $z = -1000\text{m}$, $z = -2000\text{m}$ and $z = -3000\text{m}$.

model driving the dynamics of key hydrogeological variables, i.e., porosity, pressure head, and temperature distribution. The advantage of adopting a GPCE-based analysis of the random system response is that the GPCE is linked directly to the variance-based Sobol indices and provides a surrogate model of the random system states. This can then be employed to perform detailed and computationally affordable assessment of uncertainty propagation through the numerical model. A sparse-grid-based interpolation technique has been implemented for the computation of the GPCE reduced model. When compared against typically adopted Monte Carlo sampling strategies, the use of sparse grids allows obtaining reliable results at an affordable computational cost.

- The procedure and technique proposed are exemplified through a one-dimensional application focusing on quartz cementation and depicting the geochemical and mechanical feedback during diagenetic porosity reduction in a sandstone sedimentary basin. The relative contribution of the selected uncertain parameters and boundary conditions to the total variance of the random system outputs is analyzed through the calculated Sobol indices.

As an example, the vertical distribution of porosity at large simulation steps (a) is influenced by the sea bathymetry and by mechanical compaction within the upper portion of the basin, while (b) the parameters linked to the adopted quartz precipitation kinetic have the largest impact in the deepest regions, and (c) the effect of the activation temperature of the reaction is observed only locally at intermediate depths. The vertical variability of temperature distribution is associated with the different thermal diffusivities of the solid and liquid phases and is therefore intimately connected with porosity distribution. Note that the simplified scheme adopted relies on homogeneous material distribution within the system and does not allow evidencing significant effects of geochemical compaction on pressure distribution. A significant extension of the methodology to include different geochemical compaction processes, such as smectite-illite transformation in the presence of heterogeneous geomaterials in two- and three-dimensions will be the subject of future investigations.

- The probability density function (pdf) of porosity, pressure and temperature fields have been calculated on the basis of the obtained GPCE. With reference to simulation results at the final time, our choice of uniformly distributed uncertain model parameters and boundary conditions results in a progressive transition of the pdf of porosity from a symmetric through an asymmetric functional format with depth, as the parameters driving geochemical compaction come into play. Temperature pdf exhibits a similar behavior. Conversely, the pdf of pressure does not appear to vary with depth, possibly due to the observed dependence of pressure on a single parameter.

References

- [1] Abercrombie, H.J., Hutcheon, I.E., Bloch, J.D., de Caritat, P.: Silica activity and the smectite-illite reaction. *Geology* **22**, 539–542 (1994)
- [2] Archer, G.E.B., Saltelli, A., Sobol, I.M.: Sensitivity measures, anova-like techniques and the use of bootstrap. *Journal of Statistical Computation and Simulation* **58**(2), 99–120 (1997)
- [3] Babuška, I., Chatzipantelidis, P.: On solving elliptic stochastic partial differential equations. *Comput. Methods Appl. Mech. Engrg.* **191**(37-38), 4093–4122 (2002)
- [4] Bäck, J., Nobile, F., Tamellini, L., Tempone, R.: Stochastic spectral Galerkin and collocation methods for PDEs with random coefficients: a numerical comparison. In: J. Hesthaven, E. Ronquist (eds.) *Spectral and High Order Methods for Partial Differential Equations, Lecture Notes in Computational Science and Engineering*, vol. 76, pp. 43–62. Springer (2011).

Selected papers from the ICOSAHOM '09 conference, June 22-26, Trondheim, Norway

- [5] Barthelmann, V., Novak, E., Ritter, K.: High dimensional polynomial interpolation on sparse grids. *Adv. Comput. Math.* **12**(4), 273–288 (2000)
- [6] Beck, J., Nobile, F., Tamellini, L., Tempone, R.: On the optimal polynomial approximation of stochastic PDEs by Galerkin and collocation methods. MOX-Report 2011-23, MOX - Department of Mathematics, Politecnico di Milano (2011). Submitted
- [7] Bjorkum, P.A.: How important is pressure in causing dissolution of quartz in sandstones? *J. Sed. Resear.* **66**, 147–154 (1996)
- [8] Bjorlykke, K.: Fluid-flow processes and diagenesis in sedimentary basins. *Spec. Publ. Geol. Soc. Lon.* **78**, 127–140 (1994)
- [9] Bjorlykke, K., Hoeg, K.: Effects of burial diagenesis on stresses, compaction and fluid flow in sedimentary basins. *Mar. and Petrol. Geol.* **14**, 267–276 (1997)
- [10] Brezzi, F., Fortin, M.: Mixed and hybrid finite element methods. Springer-Verlag New York, Inc., New York, NY, USA (1991)
- [11] Buller, A.T., Bjorkum, P.A., Nadeau, P., Walderhaug, O.: Distribution of hydrocarbons in sedimentary basins. Statoil ASA, Res and Techn. Memoir **7**, 1–15 (2005)
- [12] Bungartz, H., Griebel, M.: Sparse grids. *Acta Numer.* **13**, 147–269 (2004)
- [13] Chen, Z., Ewing, R.E., Lu, H., Lyons, S.L., Maliassov, S., Ray, M.B., Sun, T.: Integrated two-dimensional modeling of fluid flow and compaction in a sedimentary basin. *Computational Geosciences* **6**, 545–564 (2002)
- [14] Constantine, P., Eldred, M., Phipps, E.: Sparse pseudospectral approximation method. ArXiv repository item number: arXiv:1109.2936v1 (2011)
- [15] Dempster, A.P.: Upper and lower probabilities induced by a multivalued mapping. *Ann. Math. Statist.* **38**, 325–339 (1967)
- [16] Fajraoui, N., Ramasomanana, F., Younes, A., Mara, T., Ackerer, P., Guadagnini, A.: Use of global sensitivity analysis and polynomial chaos expansion for interpretation of non-reactive transport experiments in laboratory-scale porous media. *Water Res. Resear.* **47**(2), W02,521 (2011)
- [17] Gautschi, W.: *Orthogonal Polynomials: Computation and Approximation*. Oxford University Press, Oxford (2004)

- [18] Ghanem, R.G., Spanos, P.D.: Stochastic finite elements: a spectral approach. Springer-Verlag, New York (1991)
- [19] Giles, M., Indrelid, S.L., Beynon, G.V., Amthor, J.: The origin of large-scale quartz cementation: evidence from large data sets and coupled heat-fluid mass transport modelling. *Spec. Publs Int. Ass. Sediment.* **29**, 21–38 (2000)
- [20] Hadipriomo, F.: Fuzzy sets in Probabilistic Structural Mechanics. In: C. Sundrarajan (ed.) *Probabilistic Structural Mechanics Handbook: Theory and Industrial Applications*, pp. 280–316. Chapman and Hall (1995)
- [21] Kleiber, M., Hien, T.D.: The stochastic finite element method. John Wiley & Sons Ltd., Chichester (1992). Basic perturbation technique and computer implementation, With a separately available computer disk
- [22] Klir, G.J., Yuan, B.: Fuzzy sets and fuzzy logic. Prentice Hall PTR, Upper Saddle River, NJ (1995). Theory and applications, With a foreword by Lotfi A. Zadeh
- [23] Land, L.S., Dutton, S.P.: Cementation of a Pennsylvanian deltaic sandstone: Isotopic data. *Journal of Sedimentary Research* **48** (1978)
- [24] Lander, R.H., Walderhaug, O.: Predicting porosity through simulating sandstone compaction and quartz cementation. *AAPG Bulletin* **83(3)** (1999)
- [25] Le Maître, O.P., Knio, O.M.: Spectral methods for uncertainty quantification. Scientific Computation. Springer, New York (2010). With applications to computational fluid dynamics
- [26] Mello, U.T., Rodrigues, J.R.P., Rossa, A.L.: A control-volume finite-element method for three-dimensional multiphase basin modeling. *Marine and Petroleum Geology* **26**, 504–518 (2009)
- [27] Milliken, K.L.: Late diagenesis and mass transfer in sandstone-shale sequences. *Treatise on Geochemistry* **7**, 115–158 (2004)
- [28] Mullis, A.M.: The role of silica precipitation kinetics in determining the rate of quartz pressure solution. *J. Geophys. Resear.* **26**, 69–112 (1991)
- [29] Oelkers, E.H., Bjorkum, P.A., Murphy, W.M.: The mechanism of porosity reduction, stylolite development and quartz cementation in North Sea sandstone. In: *Water-Rock Interaction*, pp. 1183–1186 (1992)
- [30] Oelkers, E.H., Bjorkum, P.A., Murphy, W.M.: A petrographic and computational investigation of quartz cementation and porosity reduction in North Sea sandstones. *Amer. J. of Science* **296**, 420–452 (1996)

- [31] Quarteroni, A., Sacco, R., Saleri, F.: Numerical mathematics, *Texts in Applied Mathematics*, vol. 37, second edn. Springer-Verlag, Berlin (2007)
- [32] Ramm, M.: Porosity-depth trends in reservoir sandstones: theoretical model related to Jurassic sandstones offshore Norway. *Mar. and Petrol. Geol.* **9**, 553–567 (1992)
- [33] Sageman, B.B., Lyons, T.W.: Geochemistry of fine-grained sediments and sedimentary rocks. *Treatise on Geochemistry* **7**, 115–158 (2004)
- [34] Saltelli, A., Ratto, M., Tarantola, S., Campolongo, F.: Sensitivity analysis practices: strategies for model based inference. *Reliab. Eng. Syst. Saf.* **91**, 1109–1125 (2006)
- [35] Shafer, G.: A mathematical theory of evidence. Princeton University Press, Princeton, N.J. (1976)
- [36] Smolyak, S.: Quadrature and interpolation formulas for tensor products of certain classes of functions. *Dokl. Akad. Nauk SSSR* **4**, 240–243 (1963)
- [37] Sobol, I.M.: Sensitivity estimates for nonlinear mathematical models. *Math. Modeling Comput. Experiment* **1**(4), 407–414 (1995) (1993)
- [38] Stephenson, L.P., Plumley, W.J., Palciauskas, V.V.: A model for sandstone compaction by grain interpenetration. *J. Sed. Petrol.* **62**, 11–22 (1992)
- [39] Sudret, B.: Global sensitivity analysis using polynomial chaos expansions. *Reliability Engineering & System Safety* **93**(7), 964 – 979 (2008). DOI DOI: 10.1016/j.res.2007.04.002
- [40] Trefethen, L.N.: Is Gauss quadrature better than Clenshaw-Curtis? *SIAM Rev.* **50**(1), 67–87 (2008)
- [41] Walderhaug, O.: Precipitation rates for quartz cement in sandstones determined by fluid-inclusion microthermometry and temperature-history modelling. *J. Sed. Resear.* **A64**, 324–333 (1994)
- [42] Walderhaug, O.: Kinetic modeling of quartz cementation and porosity loss in deeply buried sandstone reservoirs. *AAPG Bulletin* **80**, 731–745 (1996)
- [43] Walderhaug, O., Lander, R.H., Bjorkum, P.A., Oelkers, E.H., Bjolykke, K., Nadeau, P.H.: Modelling quartz cementation and porosity in reservoir sandstones: examples from Norwegian continental shelf. *Spec. Publs Int. Ass. Sediment.* **29**, 39–49 (2000)
- [44] Wangen, M.: Physical principles of sedimentary basin analysis. Cambridge University Press (2010)

- [45] Weyl, P.K.: Pressure solution and the force of cristallization—a phenomenological theory. *J. Geophys. Resear.* **64**, 2001–2025 (1959)
- [46] Wiener, N.: The homogeneous chaos. *Am. J. Math.* **60**, 897–936 (1938)
- [47] Worden, R., Morad, S.: Quartz cementation in oil field sandstone: a review of the key controversies. *Spec. Pubs Int. Ass. Sediment.* **29**, 1–20 (2000)
- [48] Xiu, D., Karniadakis, G.: The Wiener-Askey polynomial chaos for stochastic differential equations. *SIAM J. Sci. Comput.* **24**(2), 619–644 (2002)

MOX Technical Reports, last issues

Dipartimento di Matematica “F. Brioschi”,
Politecnico di Milano, Via Bonardi 9 - 20133 Milano (Italy)

- 13/2012** FORMAGGIA, L. *et al.*
Global Sensitivity Analysis through Polynomial Chaos Expansion of a basin-scale geochemical compaction model
- 12/2012** GUGLIELMI, A.; IEVA, F.; PAGANONI, A.M.; RUGGERI, F.
Hospital clustering in the treatment of acute myocardial infarction patients via a Bayesian semiparametric approach
- 11/2012** BONNEMAIN, J.; FAGGIANO, E.; QUARTERONI, A.; DEPARIS, S.
A Patient-Specific Framework for the Analysis of the Haemodynamics in Patients with Ventricular Assist Device
- 10/2012** LASSILA, T.; MANZONI, A.; QUARTERONI, A.; ROZZA, G.
Boundary control and shape optimization for the robust design of bypass anastomoses under uncertainty
- 09/2012** MAURI, L.; PEROTTO, S.; VENEZIANI, A.
Adaptive geometrical multiscale modeling for hydrodynamic problems
- 08/2012** SANGALLI, L.M.; RAMSAY, J.O.; RAMSAY, T.O.
Spatial Spline Regression Models
- 07/2012** PEROTTO, S.; ZILIO, A.
Hierarchical model reduction: three different approaches
- 06/2012** MICHELETTI, S.; PEROTTO, S.
Anisotropic recovery-based a posteriori error estimators for advection-diffusion-reaction problems
- 05/2012** AMBROSI, D.; ARIOLI, G.; KOCH, H.
A homoclinic solution for excitation waves on a contractile substratum
- 04/2012** TUMOLO, G.; BONAVENTURA, L.; RESTELLI, M.
A semi-implicit, semi-Lagrangian, p-adaptive Discontinuous Galerkin method for the shallow water equations